Organic Electronics 107 (2022) 106553

Contents lists available at ScienceDirect

Organic Electronics

journal homepage: www.elsevier.com/locate/orgel

Detailed electro-optical modeling of thermally-activated delayed fluorescent OLEDs with different host-guest concentrations

S. Sem [a,b,*], S. Jenatsch [a,**], P. Sahay [b], S. Züfle [a,c], M. Schmid [b], W. Brütting [b], B. Ruhstaller [a,c]

[a] Fluxim AG, Katharina-Sulzer-Platz 2, 8400, Winterthur, Switzerland
[b] Institute of Physics, University of Augsburg, 86159, Augsburg, Germany
[c] Zurich University of Applied Sciences, 8400, Winterthur, Switzerland

ARTICLE INFO

Keywords:
Organic light-emitting diodes
TADF
Host-guest systems

ABSTRACT

OLED device optimization often relies on time-consuming trial-and-error experiments. While the photoluminescence quantum yield can serve as a first indicator to find the best performing host-guest ratio, this quantity does not consider the impact of the latter on the charge transport in the full device. Herein, we analyse four thermally activated delayed fluorescence OLEDs with varied host-guest ratio in the emissive layer. These devices were characterized and modelled in steady-state, under transient conditions and in the frequency domain. In this set of devices charge injection into and transport inside the emissive layer plays a crucial role in the performance. Evidenced by a particular transient electroluminescence turn-off overshoot, we show that for the 5% guest concentration device electron and hole transport occurs mainly on the host molecules, with guest molecules acting as trap states. For the other devices with higher guest concentration, we find that transport occurs mainly on the guest molecules. As a second step, a fit of the luminance efficiency is performed, with which we can extract the triplet-triplet annihilation and triplet-polaron annihilation rates. By comparing the extracted parameters, we found that they increase with increasing concentration of guest molecules. Moreover, we were able to identify triplet-polaron quenching from holes to be limiting the luminance efficiency at low current, while triplet-polaron quenching from electrons and triplet-triplet annihilation are the dominant non-radiative decay processes in the high current regime. Overall, we demonstrate that model-based analysis of steady-state, transient and frequency domain data obtained for a thermally activated delayed fluorescence OLED allows to get a deeper understanding of the efficiency limiting factors for various host-guest concentrations and driving currents.

1. Introduction

Thermally-activated delayed fluorescence (TADF) OLEDs have gained the attention of both academic and industrial research in the last years [1,2]. The main property of these materials is their ability to up-convert non-radiative triplet states into radiative singlet ones, which allows moving the limit of 25% internal quantum efficiency in normal fluorescent OLEDs up to theoretically 100% [3–5]. This makes TADF OLEDs a very interesting technology for replacing fluorescent and phosphorescent emitters in today's commercial OLED products. However, the device stability and efficiency has still to be improved and is the focus of active ongoing research [6,7].

The simplest emissive layers (EMLs) of TADF OLEDs consist of the emissive TADF molecules (guest) embedded in a matrix (host). A key role, in this context, is played by the host-guest ratio, which has a strong impact on the OLED's performance. We can identify the two main processes impacted by the host-guest ratio to be: 1) modified charge injection and transport in the emissive layer [8–10] and 2) aggregation of guest molecules. Studies have shown that at high concentrations the guest molecules tend to form aggregates and agglomerates [11–13]. This might lead to a reduction of the external quantum efficiency (EQE) caused by the surge of second-order non-radiative decays such as triplet-triplet annihilation (TTA), singlet-polaron quenching (SQP) and triplet-polaron quenching (TPQ) [14] or concentration quenching, which reduces the photoluminescence quantum yield (PLQY) [15,16]. In addition, especially in blue-emitting compounds, the energy released

* Corresponding author. Fluxim AG, Katharina-Sulzer-Platz 2, 8400, Winterthur, Switzerland.
** Corresponding author.
E-mail addresses: stefano.sem@fluxim.com (S. Sem), sandra.jenatsch@fluxim.com (S. Jenatsch).

https://doi.org/10.1016/j.orgel.2022.106553
Received 8 February 2022; Received in revised form 11 April 2022; Accepted 11 May 2022
Available online 14 May 2022

by those loss mechanisms is large enough to cause bond cleavage and therefore a faster degradation of the device [17]. Consequently, it is extremely important to fully understand and investigate these processes and optimize the OLED accordingly.

Often, the host-guest ratio is simply optimized by time-consuming and costly trial-and-error experiments. A more elegant way would be to replace this process by combining advanced characterization techniques and subsequent predictive device simulations. This dual approach allows to gain a deeper comprehension of all relevant processes and their roles in the final performance of the OLED.

In this study we analyse a series of TADF OLEDs with systematically varied host-guest concentrations. As a first step we analysed transient electroluminescence data (TEL), from which we identified that for low concentration the emitter molecules act as trap state. With this assumption, we could quantitively simulate the steady-state, transient and impedance response of all devices at once. The final and excellent correspondence between experiments and simulations guarantees that the model has been defined in a correct way and that all the important processes are captured. Moreover, this analysis allows us to estimate the electro-optical properties of the emissive layer composed of a host-guest mixture of specific concentration. In the last section we focused our attention on the efficiency curves, where we investigated the role of TTA, TPQ-n and TPQ-p in the efficiency roll-off behaviour for each device.

We would like to emphasize the importance of analysing multiple experimental techniques. Only with this approach a reliable estimation of the modeling parameters can be obtained [18] which is a key requirement for further optimizations.

2. Fabrication

Fabrication of the devices was carried out on pre-patterned 90 nm thick Indium Tin Oxide (ITO) on glass substrates provided by Kintec. Substrate preparation for deposition includes cleaning which is carried out in clean room using Acetone and Isopropyl alcohol bath in ultrasonicator each for 10 min respectively followed by UV-Ozone treatment with a mercury lamp for 15 min. The substrates are then spin coated with PEDOT:PSS (Clevios™ PEDOT:PSS; AI 4083 from Heraeus) and dried on a hot plate for 30 min at 150° Celsius under ambient conditions to get rid of the water content. The ITO and PEDOT:PSS together act as the anode for our OLED devices. The substrates are then transported to the glovebox in wafer trays wrapped in parafilm followed by loading them in the vacuum chamber located inside the glovebox thus under Nitrogen environment.

The deposition of organic layers by thermal deposition was carried under a vacuum of 10^{-7}mbar. The device structure includes 10 nm Molybdenum Oxide (MoOx) (supplied by sigma Aldrich), 5 nm 3,3′-Di (9H-carbazol-9-yl)-1,1′-biphenyl (mCBP) (from Lumtec) and 20 nm tris (4-carbazoyl-9-ylphenyl)amine (TCTA) (from Lumtec) as hole transport side (HTL). The EML consist of 20 nm of mCBP-CN and DMAC-TRZ (both supplied by Lumtec) as host-guest system and we vary the concentration of DMAC-TRZ to 5 wt%, 10 wt%, 20 wt% and 50 wt%. This is followed by the deposition of 5 nm Bis [2-(diphenylphosphino)phenyl]ether oxide (DPEPO) (supplied by TCI) as an exciton blocking layer. For electron transport layer (ETL), we deposit 50 nm 2,2′,2′′-(1,3,5-Benzinetriyl)-tris(1-phenyl-1-H-benzimidazole) (TPBi) (from Lumtec) topped off with 0.5 nm Lithium Fluoride (LiF) (from Lumtec) and 100 nm Aluminium (supplied by Lesker) as the cathode.

3. Experimental results

In this section, the employed experimental techniques and obtained results are described and discussed. The all-in-one measurement platform Paios was used to perform all DC, AC and time-dependent optoelectronic characterization experiments [19]. Paios allows to perform the entire range of techniques without the need of changing measurement system or contacts. In this report, we show only one pixel for each OLED device, whereas in the Supporting Information document we report the JV curves for additional pixels.

3.1. Current-voltage-luminance (JVL) curves

Current-Voltage-Luminance (JVL) is the basic experiment of OLED devices. In this case we measured JV(L) with the pulsed mode available in Paios. Each point of the curve is measured by applying a voltage pulse of 40 ms and the values of I and L are taken as the average during the voltage pulse.

From the experimental results in Fig. 1a, we see that 5% emitter concentration gives a lower current with respect to all the other devices. The currents for the 10, 20 and 50% concentration are very similar, but we notice a slightly steeper turn on of the 50% device. For all devices the turn-on voltage is approx. 3.5 V.

3.2. Injection-CELIV

Injection-CELIV (charge extraction by linearly increasing voltage) is a transient experimental technique frequently used in the characterization of organic devices such as OLEDs or solar cells [20]. This technique is frequently also used for metal-insulator-semiconductor device structures, and in that case it can be referred to as MIS-CELIV [21].

Injection-CELIV allows the investigation of charge accumulation at different interfaces inside the stack as well as to estimate apparent electron and hole mobilities [22,23]. A quantitative analysis of the latter is however fairly difficult in a multi-layer device.

This experiment consists of the application of an offset (forward) voltage (V_{offset}) followed by a linearly increasing voltage ramp until a fixed (negative) voltage is reached. The measured current is composed of a displacement current with eventual additional peaks that can be assigned to extracted charge carriers which were either present inside the device beforehand or have been injected during the offset forward voltage. We performed the experiment with different V_{offset}, from 1 V to 6 V with 0.5 V step. The ramp rate is 0.1 V/μs for each of the measurements, the final voltage is -5 V.

From the experimental results we see the formation of two separate peaks in all the devices, a broad one is already visible with an $V_{offset} = 2$ V, below turn on (Fig. 1c), while the second one, much larger, appears only above turn on voltage (Fig. 1d). Note that the peak at longer times is still present in the 4.5 V experiments, even if partially covered by the initial one.

The occurrences of a peak with an $V_{offset} = 2$ V indicates the presence of charges in the devices well below the turn on voltage of the OLED. We can also remark that increasing the guest concentration causes a shift of the peak to the left i.e. to shorter carrier extraction times. Depending on which charge carrier is already present in the device, this suggests a change in the transport properties of the EML.

When using a $V_{offset} = 4.5$ V an additional, significantly larger peak can be seen. This is expected since at 4.5 V the devices are already above turn-on which occurs at approx. 3.5 V. We can also observe that the height of the peak is different for all devices. This is directly related to the amount of charges flowing through the device during the V_{offset}. This initial peak is attributed to injected charge carriers and exhibits the opposite trend in peak time vs guest concentration compared to the broad peak which is present below turn on.

3.3. Impedance spectroscopy

In impedance spectroscopy (IS) an oscillating voltage (V_{AC}) is applied to the OLED on top of a steady-state voltage (V_{DC}). The impedance Z or admittance Y can be calculated from the measured oscillating current with equation (1) [18]. In this study we focus our attention on the imaginary part of the admittance which defines the capacitance C that we plot vs. frequency or applied voltage.

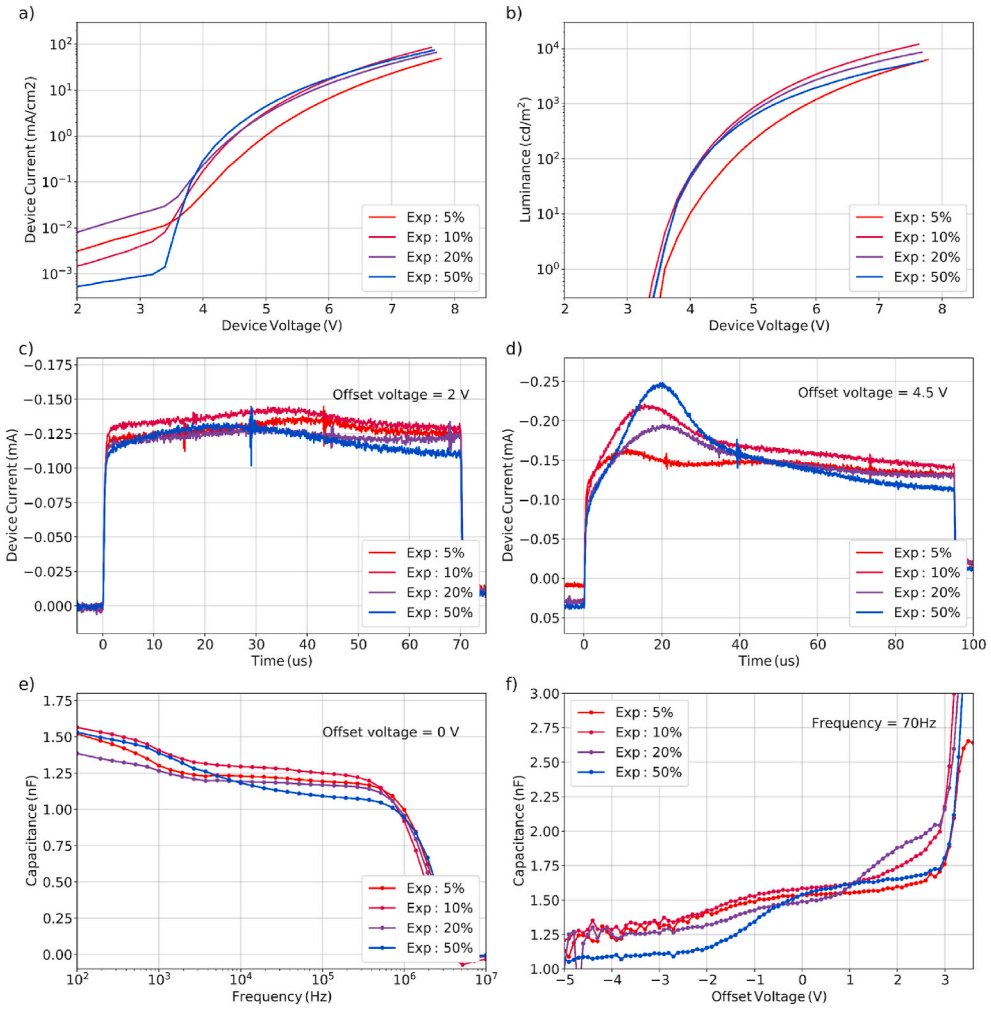

Fig. 1. Experimental results of each device: (a) JV; (b) luminance vs voltage; (c) injection-CELIV with $V_{offset} = 2$ V; (d) injection-CELIV with $V_{offset} = 4.5$ V; (e) C-f with $V_{offset} = 0$ V; (f) C–V with frequency = 70 Hz.

$$\overline{Y} = \frac{1}{\overline{Z}} = \frac{I_{AC}}{V_{AC}} = G + i2\pi fC \quad (1)$$

here we measured IS in different conditions: keeping V_{DC} fixed while varying the frequency (C-f), or the opposite, keeping the frequency constant while varying V_{DC} (C–V).

Fig. 1e shows the C-f plot at a fixed V_{DC} of 0 V. For all the devices the capacitance is increasing at low frequency, it reaches a plateau in the range of 10 kHz–300kHz – which is attributed to the geometrical capacitance of the (empty) device – and then decreases sharply at 1 MHz because of the series resistance. The most interesting result from the C-f plot is the additional capacitance plateau present at low frequency. This result suggests that at 0 V charges are already injected into the stack and accumulate at a particular interface.

Fig. 1f shows the C–V plot at a fixed frequency of 70 Hz. For all the devices we see a similar effect, at low bias, below -2 V, we see the geometric capacitance (C_{geo}, with values in the range of 1.1–1.3 nF for all the devices); with increasing voltage we can see a clear transition from C_{geo} to a plateau (C_{plat}) at a transition voltage (V_t) of roughly -2 V, suggesting the injection of charges already at this negative bias; finally, above 3 V, we see a sharp increase of capacitance followed by a drop, which indicates injection of electrons and holes and subsequent recombination.

From Fig. 1f we can see that the 50% device has a slightly lower geometrical capacitance. This is an indication that this device has an unintentionally larger thickness. However, this small difference does not affect the overall results of this study.

3.4. Analysis of C–V results

From the experimental C–V shown in Fig. 1f, we see the presence of capacitance plateaus occurring between 0 V and 1 V, at slightly different voltage for each device. The increase of capacitance below 0 V is a clear signature of the presence of one or multiple polar layers [22–25]. Assuming a permittivity of 3 we calculated the thicknesses associated to the plateaus (Table 1) from the formula $C = \mathscr{E}_0 \mathscr{E}_r A/d$.

According to the nominal thickness described in the fabrication paragraph we can see that the thickness of TPBi + DPEPO is 55 nm and EML + TPBi + DPEPO is 75 nm. The interpretation is that for all the devices there is an early injection of holes starting at around -2 V which accumulate at the TCTA/EML or EML/DPEPO interface. Simulations described in the next chapter and in SI confirm this hypothesis.

Additionally, there are three aspects that we want to comment

Table 1
Calculated thickness associated to plateau in CV experimental results.

Device	Plateau	Calculated thickness
5%	1.55 nF	68 nm
10%	1.60 nF	66 nm
20%	1.50 nF	70 nm
50%	1.65 nF	65 nm

briefly. First, at reversed bias the 50% device shows a lower C_{geo} with respect to the other devices which can be attributed to an unintended larger thickness of this device. Second, the device with 20% concentration shows an additional shoulder starting at 1 V. At the moment, we cannot explain this feature in detail. We speculate that at 1 V holes already accumulated at the TCTA/EML or EML/DPEPO interface are able to overcome it, which would result in an increased capacitance. This feature could not yet be reproduced in our simulations but is further investigated. It is also worth to mention that this feature disappears for C–V measurements at different frequencies. Third, in 50% device the capacitance shift from C_{geo} to C_{plat} occurs at −1 V, slightly higher than the other devices. It could be explained by considering a different polarity of the EML in this device, as explained in section 4.4.

3.5. Transient electroluminescence

Transient electroluminescence (TEL) is performed by applying a voltage step to the OLED while measuring the emitted light and the respective current. We performed TEL with an offset voltage of -5 V and a pulse duration of 500us (Fig. 2a-inset). This experiment was performed with different pulse height, from 3 V to 7 V.

In Fig. 2a, the normalized emission decay of the four devices is shown with a voltage pulse of 6 V. From the experimental result it is important to note that in the 5% device a clear overshoot in the first 2–3 us of the turn-off electroluminescence decay is observed, while the other three samples show a monotonic decay.

This overshoot has already been investigated by Regnat et al. [26] and attributed to emission zone splitting. In this publication Regnat et al. explained that during steady state charges accumulate at the respective blocking layers inside the EML and once the voltage switches to reverse bias electrons and holes start flowing backwards to Al and ITO, respectively, thereby a large number of electrons and holes will meet approximately in the middle of the EML, giving rise to the short-lived TEL overshoot. Although this explanation cannot be ruled out completely, it is difficult to reason why this effect is here only present in the 5% device.

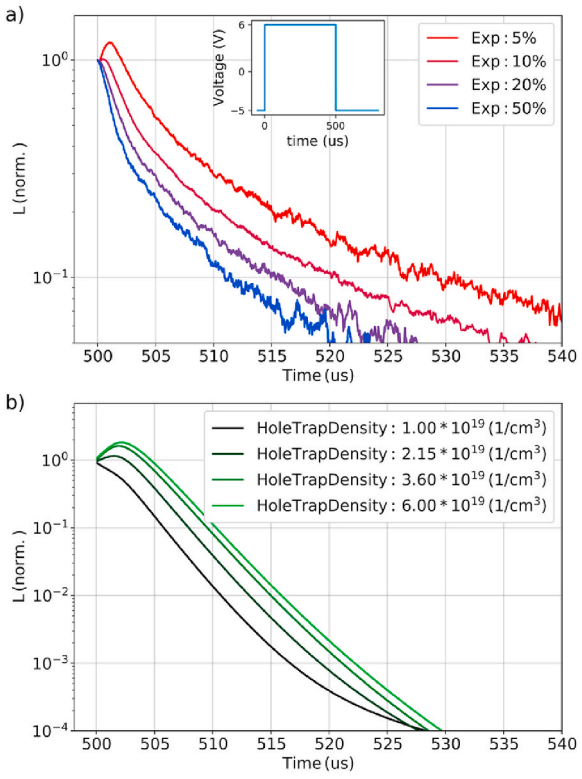

Fig. 2. Transient EL analysis: (a) experimental TEL turn-off normalized emission with a voltage pulse of 6 V (inset: schematics of the applied voltage pulse); (b) simulated TEL turn-off normalized emission with different hole trap density in the EML.

In previous work, this TEL overshoot after turn-off has alternatively been explained by the presence of trap states [27]. Indeed, we can reproduce this effect with simulations by including traps in the EML. Fig. 2b shows that an increased trap density in the EML give rise to a TEL overshoot. Additional details of these simulations are shown in the SI, where we analysed the charge density profile at different timesteps after the voltage turn-off. This simulation was performed on a simplified stack, different from the one indicated in chapter 4. This result is an indication that for 5% the guest molecules in the EML act as trap states, while for higher concentration they don't.

4. Simulations

To analyse and understand the results described in the experimental section, we modelled the device behaviour with the simulation software Setfos [28]. Setfos allows to perform electrical simulations based on the drift-diffusion approach (in steady state, transient and frequency-domain), as well as electro-optical simulations based on the dipole emission and transfer-matrix models [18].

In these sections the key physical processes governing these OLEDs are discussed and explained with the support of simulations. The final simulations are performed with the parameters indicated in Table 2 and the resulting plots are shown in Fig. 4.

The modelled stack is presented in Fig. 3. We must note that with Setfos we cannot include different molecular species in one layer and therefore the EML is modelled with an effective HOMO/LUMO energy level and electron/hole mobility. Another approximation done in the study is related to the presence of multiple polar layers inside the stack (DPEPO, mCBPCN and TPBi). For simplicity, we consider in simulations only TPBi to be polar (apart from the device 50%, where the polarity of the EML appears to play an important role, see chapter 4.4).

4.1. Charge transport in the EML

Before going into detail about the modeling of the different devices,

Table 2
In the "Reference" column the values from literature are indicated. The actual values used in simulation are indicated in the "Used in simulation" column.

Parameter	Reference	Used in simulation
Hole injection barrier (eV)	–	0.2
TCTA HOMO LUMO level (eV)	[29] 5.8/2.4	5.8/2.4
TCTA hole mobility ($cm^2V^{-1}s^{-1}$)	[35] 3×10^{-4}	3×10^{-4}
TCTA electron mobility ($cm^2V^{-1}s^{-1}$)	–	1×10^{-6}
DPEPO HOMO LUMO level (eV)	[36] 6.1/2.0	6.1/2.25
DPEPO hole mobility ($cm^2V^{-1}s^{-1}$)	–	1×10^{-9}
DPEPO electron mobility ($cm^2V^{-1}s^{-1}$)	[37] 5.62×10^{-6}	5.62×10^{-6}
TPBi HOMO LUMO level (eV)	[38,39] (6.2–6.7)/2.7	6.5/2.5
TPBi hole mobility ($cm^2V^{-1}s^{-1}$)	–	10^{-6}
TPBi electron mobility ($cm^2V^{-1}s^{-1}$)	[40] 3.16×10^{-5}	3.16×10^{-5}
TPBi sheet charge density (mC/m^2)	[41]0.93–1.1 [42];1.4 [43];2.6	2.64
TPBi electron trap density (cm^{-3})	–	5.48×10^{18}
TPBi electron trap depth (eV)	–	0.225
TPBi electron trap capture rate (cm^3s^{-1})	–	10^{-10}
Electron injection barrier (eV)	–	0.1
DMAC-TRZ HOMO LUMO level (eV)	–	See Table 3
mCBPCN HOMO LUMO level (eV)	6.1/2.5	See Table 3

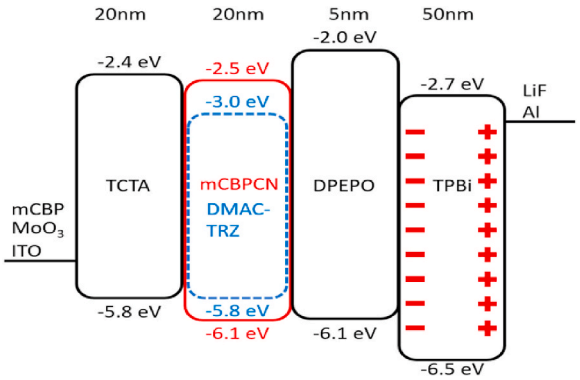

Fig. 3. Device structure considered in simulation. TPBi has been assumed to be the only polar layer in the stack for 5-10-20% devices. The energy levels indicated in the image are the ones found in literature, see Table 2.

we tackle the process of charge transport in the EML, which is concentration-dependent. As seen from the energetic diagram in Fig. 3, there is a significant HOMO/LUMO energy difference between the host and the guest molecules. It is reasonable to infer that for small guest concentrations, the guest molecules act as trap states. In this case the large distance between guest molecules precludes any transport among them. Increasing the dye dopant concentration, the distance between guest molecules decreases, allowing charge transport via the guest molecules [29]. With the support of the TEL simulation's result, we can identify two distinct regimes depending on the guest concentration: the "low concentration" regime, where transport occurs on the host molecules and the guest molecules act as trap states, and the "high concentration" regime, where injection and transport occurs on the guest molecules. To replicate these two regimes in simulations, we assume the HOMO/LUMO energy levels of the EML to be similar to the guest (host) ones and exclude (include) trap states in case of high (low) guest concentration. The "low concentration" regime is applied to the device with 5% guest concentration while the "high concentration" regime to all the other devices (see Table 3).

4.2. Additional simulation details

From the previous sections we see that in multiple experiments there is an initial injection of charges in the stack already at negative bias (injection-CELIV, IS (C-f, C–V)). These results suggest the presence of a polar layer. As described by W. Brütting et al. [25], having a polar layer inside the stack introduces an additional (fixed) electric field inside the polar layer. The origin of this electric field is spontaneous orientation polarization and it can be expressed by a net positive and negative sheet charge density at the two extremities of the layer. This phenomenon can be simulated with Setfos as described in S. Altazin et al. [24] with the use of two thin boundary layers with positive and negative carrier doping.

Modeling of TPBi plays a crucial role in these simulations. TPBi molecules possess a large permanent dipole moment, which - combined

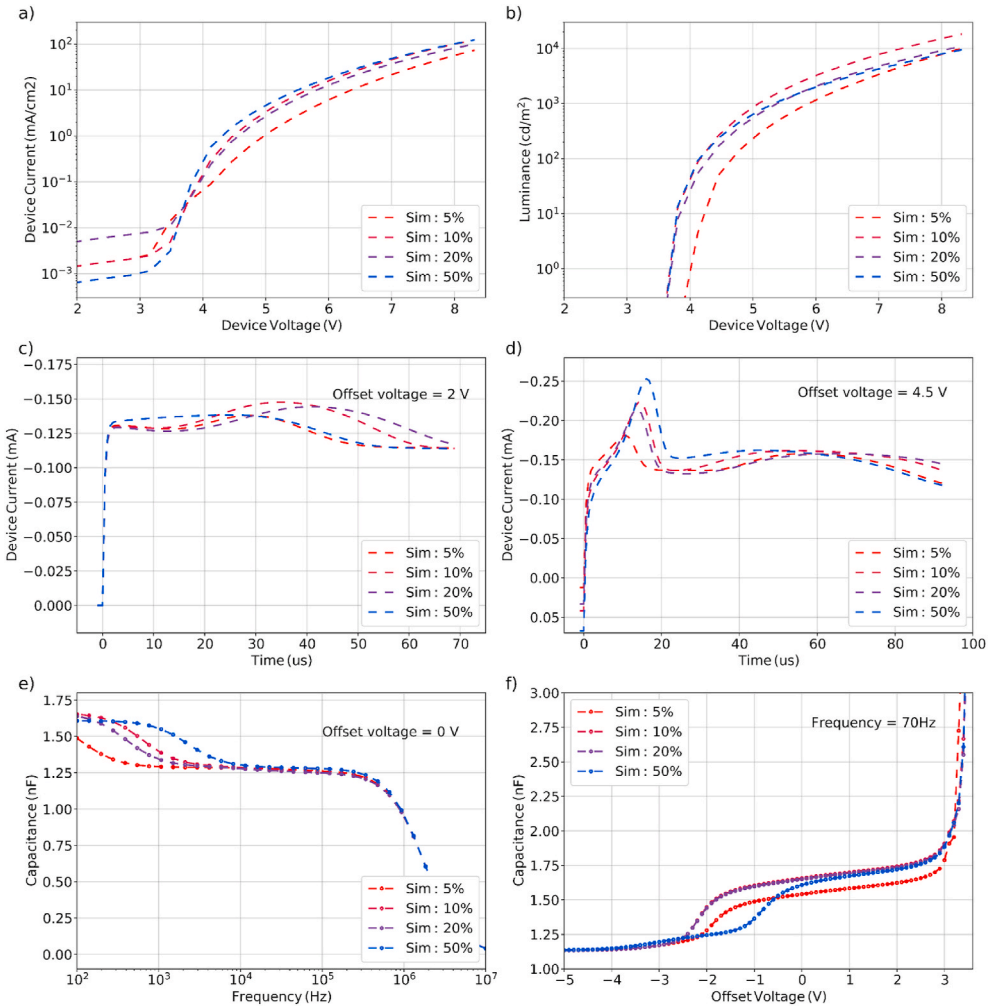

Fig. 4. Simulation results of each device: (a) JV; (b) luminance vs voltage; (c) injection-CELIV with $V_{offset} = 2$ V; (d) injection-CELIV with $V_{offset} = 4.5$ V; (e) C-f with $V_{offset} = 0$ V; (f) C–V with frequency = 70 Hz.

Table 3
EML parameters used in simulations.

Parameter	5%	10%	20%	50%
EML HOMO LUMO level (eV)	6.00/ 2.25	5.9/3	5.9/3	5.9/3
EML zero field hole mobility ($cm^2V^{-1}s^{-1}$)	7×10^{-7}	3.87×10^{-7}	2.44×10^{-7}	2.7×10^{-7}
EML field-enhancement coefficient-for holes ($m^{1/2}V^{-1/2}$)	4.64×10^{-5}	4.64×10^{-5}	4.64×10^{-5}	4.64×10^{-5}
EML zero field electron mobility ($cm^2V^{-1}s^{-1}$)	10^{-6}	6×10^{-7}	3×10^{-7}	4.37×10^{-7}
EML field-enhancement coefficient-for electrons ($m^{1/2}V^{-1/2}$)	2×10^{-5}	2×10^{-5}	2×10^{-5}	2×10^{-5}
EML sheet charge density (mC/m^2)	–	–	–	−0.7
EML electron trap density (cm^{-3})	10^{17}	–	–	–
EML electron trap depth (eV)	0.75	–	–	–
EML electron trap capture rate (cm^3s^{-1})	10^{-12}	–	–	–
EML hole trap density (cm^{-3})	10^{17}	–	–	–
EML hole trap depth (eV)	0.2	–	–	–
EML hole trap capture rate (cm^3s^{-1})	10^{-12}	–	–	–

with a strong molecular orientation - induce the whole layer to be polar. According to Coehoorn et al. [30], a direct consequence of the strong dipole moment of TPBi is that electron transport is highly dispersive. We modelled these two effects separately in Setfos: polarity can be recreated with fixed positive and negative charge densities at the two extremities of TPBi, as described above, while the dispersive transport is considered by adding trap states for electrons. In the SI a brief analysis to clarify the necessity to introduce trap states in TPBi is described.

The excitonic parameters used in simulations are indicated in Table 4, and they are estimated from transient PL experiments with use of a specific fitting procedure [31]. Details about the method and experimental results are shown in the SI.

In our simulation (Setfos), the excitonic model is implemented with customizable 1D rate equations which are fully coupled to the charge densities obtained from the drift-diffusion model [32,33]. For each exciton, several parameters must be defined: generation coefficient, radiative decay rate, non-radiative decay rate, triplet-triplet annihilation rate, singlet-singlet annihilation rate and optionally other parameters. We can distinguish mono-molecular (like radiative, non-radiative, intersystem crossing, …) and bi-molecular (like triplet-triplet annihilation, triplet-polaron quenching, …) excitonic rates. The first type does not depend on the exciton or charge density, and therefore the unit of these rates is s^{-1}, while the second instead depends on the exciton or charge density, and the unit, in this case, is cm^3s^{-1}. Alternatively, for further in-depth analysis and consideration of long-range interactions across nearest neighbours and layer interfaces a 3D master equation model for exciton dynamics is available in Setfos [34]. The use of this hybrid and coupled 1D drift-diffusion and 3D master equation model is beyond the scope of this paper and will be subject of follow-up work.

Table 4
Excitonic parameter extracted from TrPL fitting (see SI).

Parameter	5%	10%	20%	50%
Radiative decay – singlet (s^{-1})	2.38×10^7	2.06×10^7	2.12×10^7	1.81×10^7
Intersystem crossing rate (s^{-1})	2.92×10^7	2.68×10^7	2.46×10^7	2.34×10^7
Reverse intersystem crossing rate (s^{-1})	7.5×10^5	7.5×10^5	8×10^5	8.3×10^5
Generation efficiency – singlet	0.25	0.25	0.25	0.25
Generation efficiency – triplet	0.75	0.75	0.75	0.75

4.3. Simulation parameters

The simulation software requires several input parameters such as the refractive indices, the layer thicknesses, HOMO/LUMO energy levels and electron/hole mobilities. In Table 2 all the values used in simulations are indicated. Obviously, the material parameters of the mixed host-guest EML with various concentrations has not been characterized before in detail. Therefore, one of the goals of this study is to be able to provide an estimation for the electrical material parameters by optimizing the agreement between experimental and simulation results. The extracted parameters of the EML layer are shown in Table 3. The excitonic parameters were extracted from transient PL performed on films (see Table 4).

4.4. Effect of polarity and focus on 50%

Assuming TPBi to be the only polar layer [44], with simulations we obtain a good agreement for all the experiments for 5-10-20% devices. We extracted a sheet charge density of 2.64 mC/m^2 (positive charge at the TPBi/Al and negative at the DPEPO/TPBi). Having a polar layer inside the stack influences the entire electrical characteristic of the OLED, but the clearest evidence is visible in C–V, C-f and injection-CELIV. In C–V there is a negative V_t, in C-f ($V_{offset} = 2$ V) an increase of capacitance is visible at low frequency and in injection-CELIV ($V_{offset} = 2$ V) a clear peak is present, indicating the extraction of accumulated charges. In Fig. 4 we can see that all the three results are well reproduced by simulations. Further simulation results are indicated in SI, where the charge profile is analysed at different voltage, clearly showing that the accumulation of holes occurs mainly at the TCTA/EML and EML/DPEPO interface.

In the device with 50% guest concentration we see three main differences with respect to the other devices: in JV there is a slightly lower current turn-on, in capacitance-voltage V_t is shifted from −2 to -1 V and in injection-CELIV with $V_{offset} = 2$ V the rise attributed to hole accumulation starts at 0 us (as soon as the linear reversed ramp is applied). All these experimental results indicate a different polarity effect in this device, and as the only difference to the other devices is the EML, our initial approximation supposing a non-polar EML does not hold anymore. Since both the host (mCBP-CN) and the guest molecules (DMAC-TRZ) possess a permanent dipole moment, it is challenging to understand the role of increasing guest concentration. One could assume that in 5%–10%–20% devices the EML possess a certain polarity which is reduced when increasing guest concentration to 50%. In our case, having assumed 5%-10%–20% to have a non-polar EML, we suppose the EML with 50% to be polar and the best agreement with the experimental results is obtained with a sheet charge density of −0.7 mC/m^2 (opposite direction with respect to TPBi). From Fig. 5, we see the comparison of the experimental results and simulations considering a polar and non-polar EML for device 50%. Clearly, this additional complexity in the model is required to explain the various measurements.

4.5. Analysis of efficiency roll-off

The efficiency roll-off is the result of an interaction of many processes: triplet-triplet annihilation (TTA), singlet-triplet annihilation (STA), singlet-singlet annihilation (SSA), triplet-polaron quenching with electrons (TPQ-n), triplet-polaron quenching with holes (TPQ-p), singlet-polaron quenching with electrons (SPQ-n) and singlet-polaron quenching with holes (SPQ-q) [45].

In TADF emitters the population of triplets is usually larger than the population of singlets and this causes density-dependent annihilation processes involving triplets (TTA, TPQ-n and TPQ-p) to be the most critical processes influencing the efficiency roll-off [46,47]. For this reason we will include only them in our model. In some cases also SPQ has been found to play an important role, however we assume it to be absent in this study.

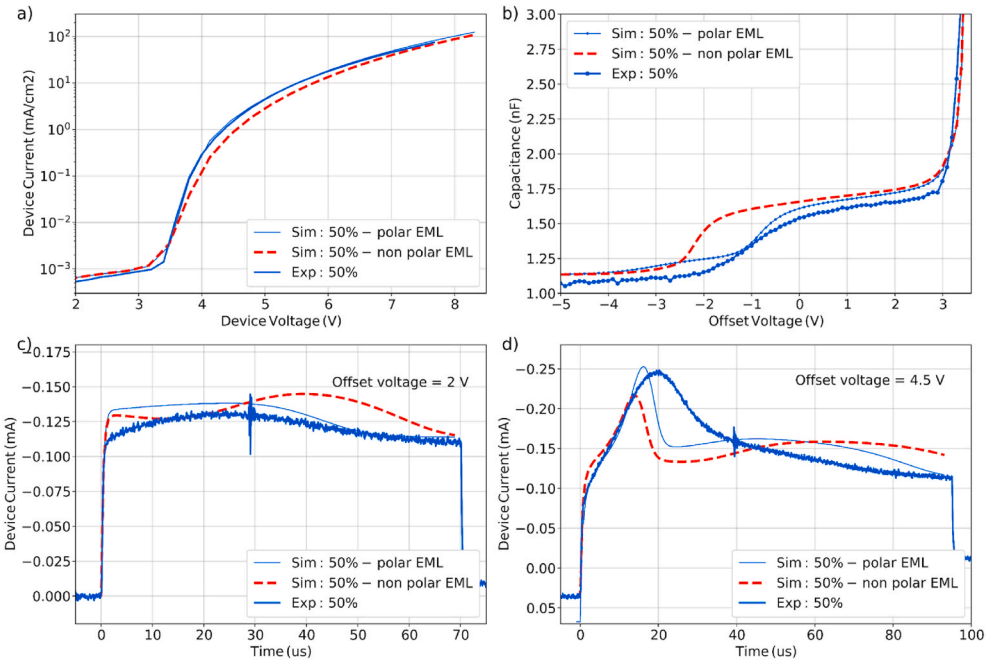

Fig. 5. Experimental and simulated results of device with 50% guest concentration considering the EML polar and non-polar. (a) JV; (b) C–V with frequency = 70 Hz; (c) injection-CELIV with V_{offset} = 2 V; (d) injection-CELIV with V_{offset} = 4.5 V.

Estimating those rates from a roll-off curve has been done in several studies [48,49], but we are aware that being able to distinguish those rates from a simple roll-off curve can be challenging. Nevertheless, we performed a fit of the luminance efficiency for all the devices, leaving the three parameters free for each device. In this way, for each device, a set of three parameters is extracted (TTA, TPQ-n and TPQ-p rates). The resulting fit is shown in Fig. 6a. At high currents, the fit well replicates all the experimental results, while for low currents the 5% simulation shows a lower efficiency. The reason could be that we modelled the 5% device such that transport in the EML occurs purely on the host molecules. It might be that a small amount of charge can be injected directly on the guest molecules even with only 5% concentration. In this case, the energy barrier between ETL and EML is reduced, and the emission starts at lower voltage. In Fig. 6b the correlation matrix of the resulting fit is shown for the 10% device. As we can see, the correlation is relatively high especially for TTA and TPQ-n ($\rho_{TTA\text{-}TPQ\text{-}n}$ (10%) = 0.92). This result is an indication that it is rather difficult to distinguish the two effects separately, which makes the specific extracted numbers not extremely solid. TPQ-p shows instead an acceptable correlation with the other two effects. The reason is that we found the TPQ-p to have a greater impact on the luminance efficiency curve at lower currents while TTA and TPQ-n rates affect the curves at higher currents. This effect is totally in line with what we described above, the polarity of TPBi induces an injection of holes already below turn-on voltage and the high

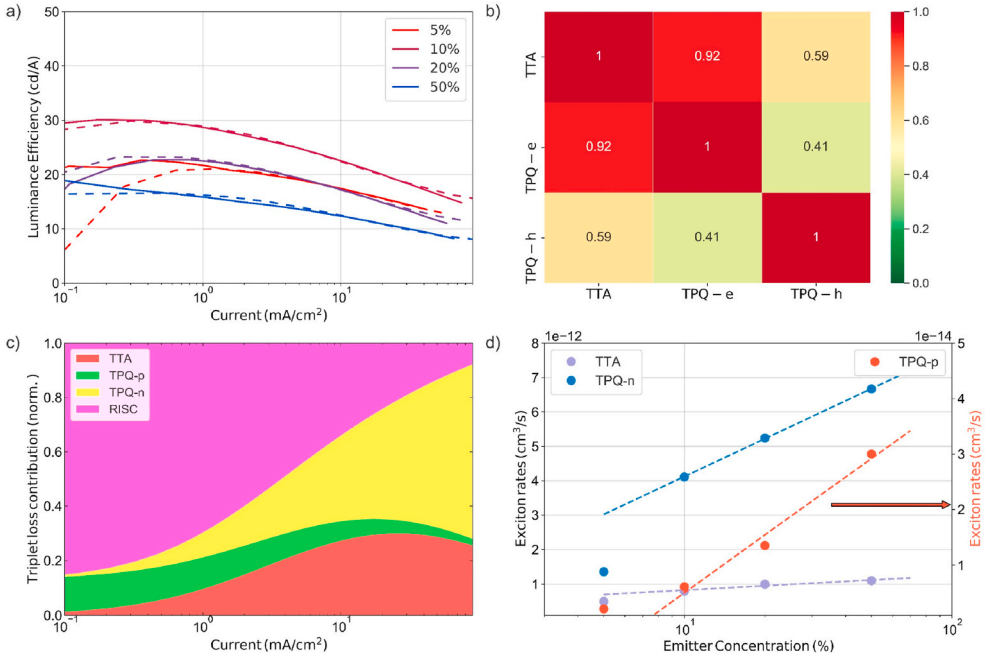

Fig. 6. The efficiency roll-off is analysed. a) Experimental data (solid line) and fit (dashed line) of the luminance efficiency roll-off for all the devices; b) correlation matrix of the luminance efficiency roll-off fit shown in a) for device 10%; c) plot of the triplet exciton losses contribution of device 10%, direct output of Setfos; d) The extracted TTA, TPQ-n and TPQ-p are plotted vs guest concentration of the EML in a log-lin scale; the dashed line indicates the fitting performed with equation (2). The fitted coefficient c_1 and c_2 are indicated in Table 5.

density of holes already at low voltage causes the TPQ-p to be the prevalent loss mechanism at low currents.

This effect can be easily identified using the exciton losses plot, which is a direct output from Setfos 5.2. In Fig. 6c we see the different contributions to triplet losses for the 10% concentration device. At low currents, we see that the dominant loss is coming from TPQ-p while at higher currents TTA and TPQ-n give a much larger contribution.

The plot in Fig. 6d displays the extracted values of TTA, TPQ-n and TPQ-p for the four devices. We can observe that all the three rates are increasing with concentration. In particular, we find an empirical logarithmic relation with the concentration for concentration higher than 5%. Equation (2) was used to produce the fit in Fig. 6d. Table 5 provides the resulting c1 and c2 values.

$$f(x) = c_1 \ln(c_2 * x) \tag{2}$$

The dependence of the TTA rate with concentration has already been investigated by Ligthart et al. [50] and Zhang et al. [51]. In both studies, they show that an increase in guest concentration produces a larger TTA rate. This happens because, at higher guest concentrations, the average distance between guest molecules decreases, and the annihilation event is facilitated.

In the case of TPQ instead, a direct relation between guest concentration and TPQ rate has not been found in the literature. An alternative possibility would be to maintain the TPQ rates concentration-independent in the fitting procedure. However, we believe that in such a case, where no direct information from literature can be found, leaving the three parameters (TTA, TPQ-n and TPQ-p) completely free to be optimized for each device is a good approach.

We would like to comment on the correlation between TTA and TPQ-n. As previously described, the effect of TTA and TPQ-n on the efficiency roll-off is very difficult to distinguish. Additional and more sophisticated experimental techniques have been performed, as described by Wehrmeister et al. [52] In this study these two processes are investigated by combining transient PL with electroluminescence. However, this type of analysis goes beyond the scope of our study.

5. Conclusions

In this contribution we have shown that charge transport in host-guest TADF emitter layers can electrically be modelled within two distinct regimes depending on the concentration of the TADF guest molecules (high and low guest concentration regimes). This approach allows us to explain the presence of transient EL decay overshoot in the device with 5% DMAC-TRZ guest concentration.

For all the devices we found signs of a polar ETL in several experiments: injection-CELIV, capacitance-voltage and capacitance-frequency. We could replicate all these signatures of the polar ETL with simulations, allowing for the extraction of the specific sheet charge density inherent to spontaneous orientation polarization (SOP) inside the ETL. Regarding the device with 50% DMAC-TRZ concentration we observed a different polarity of the EML, which we quantified as well.

By analysing the luminance efficiency roll-off we extracted the TTA, TPQ-n and TPQ-p rates which appear to be logarithmically dependent of the DMAC-TRZ molecule concentration in the EML. Additionally, TPQ-p appears to be the limiting factor of the luminance efficiency at low currents while TTA and TPQ-n are responsible for the luminance efficiency roll-off at high currents. Thanks to this comprehensive characterization we can link the strong influence of TPQ-p on the efficiency at low current with the polarity of the ETL. The strong polarity of TPBi induces a high density of holes in the EML at low voltage and, since TPQ-p depends on the hole density, this causes the effect of TPQ-p on the efficiency to be non-negligible even at low current/voltage.

This comprehensive study which includes electronic, excitonic and optical aspects, provides a basis for upcoming work on simulation based guest concentration optimization in a complete OLED device.

Table 5
Extracted coefficient of equation (2); the fit is shown in Fig. 6d.

	c_1 (cm^3/s)	c_2
TTA	1.8×10^{-13}	9.31
TPQ-n	1.6×10^{-12}	1.33
TPQ-p	1.5×10^{-14}	0.14

Declaration of competing interest

The authors declare that they have no known competing financial interests or personal relationships that could have appeared to influence the work reported in this paper.

Acknowledgements

We acknowledge funding from the Marie Skłodowska-Curie Actions via the Innovative Training Network (ITN) TADFlife (GA 812872), as well as by Schweizer Nationalfonds (SNF) and Deutsche Forschungsgemeinschaft (DFG) through the bilateral project “CTDyn”, project no. 432420985.

Appendix A. Supplementary data

Supplementary data to this article can be found online at https://doi.org/10.1016/j.orgel.2022.106553.

References

[1] M. Regnat, K.P. Pernstich, K.H. Kim, J.J. Kim, F. Nüesch, B. Ruhstaller, Adv. Electronic. Mater. 6 (2020) 1–8.
[2] C. Mayr, S.Y. Lee, T.D. Schmidt, T. Yasuda, C. Adachi, W. Brütting, Adv. Funct. Mater. 24 (2014) 5232–5239.
[3] A. Endo, K. Sato, K. Yoshimura, T. Kai, A. Kawada, H. Miyazaki, C. Adachi, Appl. Phys. Lett. 98 (2011) 2011–2014.
[4] H. Nakanotani, T. Higuchi, T. Furukawa, K. Masui, K. Morimoto, M. Numata, H. Tanaka, Y. Sagara, T. Yasuda, C. Adachi, Nat. Commun. 5 (2014) 1–7.
[5] T.J. Penfold, F.B. Dias, A.P. Monkman, Chem. Commun. 54 (2018) 3926–3935.
[6] P.L. dos Santos, J.S. Ward, M.R. Bryce, A.P. Monkman, J. Phys. Chem. Lett. 7 (2016) 3341–3346.
[7] L.S. Cui, S. bin Ruan, F. Bencheikh, R. Nagata, L. Zhang, K. Inada, H. Nakanotani, L. S. Liao, C. Adachi, Nat. Commun. 8 (2017) 1–8.
[8] V. Jankus, P. Data, D. Graves, C. McGuinness, J. Santos, M.R. Bryce, F.B. Dias, A. P. Monkman, Adv. Funct. Mater. 24 (2014) 6178–6186.
[9] W. Song, W. Lee, K.K. Kim, J.Y. Lee, Org. Electron. 37 (2016) 252–256.
[10] H. Soofi, M. Jabbari, IEEE Trans. Electron. Dev. 66 (2019) 3425–3432.
[11] Q. Du, W. Wang, S. Li, D. Zhang, W. Li, W. Zheng, Opt Commun. 366 (2016) 253–259.
[12] S.J. He, Z.B. Wang, D.K. Wang, N. Jiang, Z.H. Lu, Appl. Phys. Lett. 103 (2013).
[13] N. Liu, W.X. Shi, Y.M. Zhou, X.A. Cao, IEEE Electron. Device Lett. 40 (2019) 750–753.
[14] H.S. Kim, S.R. Park, M.C. Suh, Digest of Technical Papers - SID International Symposium 49 (2018) 1842–1845.
[15] Y. Kawamura, J. Brooks, J.J. Brown, H. Sasabe, C. Adachi, Phys. Rev. Lett. 96 (2006) 11–14.
[16] K.H. Kim, C.K. Moon, J.H. Lee, S.Y. Kim, J.J. Kim, Adv. Mater. 26 (2014) 3844–3847.
[17] X. Zhang, C. Fuentes-Hernandez, Y. Zhang, M.W. Cooper, S. Barlow, S.R. Marder, B. Kippelen, J. Appl. Phys. 124 (2018).
[18] S. Jenatsch, S. Züfle, B. Blülle, B. Ruhstaller, J. Appl. Phys. 127 (2020).
[19] Fluxim AG, Switzerland, see www.fluxim.com for Platform for all-in-one characterization (Paios).
[20] S. Dahlström, O.J. Sandberg, M. Nyman, R. Österbacka, Physical Review Applied 10 (2018) 1.
[21] A. Armin, G. Juska, M. Ullah, M. Velusamy, P.L. Burn, P. Meredith, A. Pivrikas, Adv. Energy Mater. 4 (2014) 1–8.
[22] S. Züfle, S. Altazin, A. Hofmann, L. Jäger, M.T. Neukom, W. Brütting, B. Ruhstaller, J. Appl. Phys. 122 (2017).
[23] S. Züfle, S. Altazin, A. Hofmann, L. Jäger, M.T. Neukom, T.D. Schmidt, W. Brütting, B. Ruhstaller, J. Appl. Phys. 121 (2017).
[24] S. Altazin, S. Züfle, E. Knapp, C. Kirsch, T.D. Schmidt, L. Jäger, Y. Noguchi, W. Brütting, B. Ruhstaller, Org. Electron. 39 (2016) 244–249.
[25] W. Brütting, S. Berleb, A.G. Mückl, Org. Electron. 2 (2001) 1–36.
[26] M. Regnat, K.P. Pernstich, S. Züfle, B. Ruhstaller, ACS Appl. Mater. Interfaces 10 (2018) 31552–31559.
[27] V. Savvate'ev, J.H. Friedl, L. Zou, J. Shinar, K. Christensen, W. Oldham, L. J. Rothberg, Z. Chen-Esterlit, R. Kopelman, Appl. Phys. Lett. 76 (2000) 1501–1503.
[28] Fluxim AG, Switzerland, see www.fluxim.com for Simulation software Setfos.

[29] Z.Q. Zhang, Y.P. Liu, Y.F. Dai, J.S. Chen, D.G. Ma, H.M. Zhang, Chin. Phys. Lett. 31 (2014).
[30] R. Coehoorn, X. Lin, C.H.L. Weijtens, S. Gottardi, H. van Eersel, Physical Review Applied 16 (2021) 1.
[31] N. Haase, A. Danos, C. Pflumm, A. Morherr, P. Stachelek, A. Mekic, W. Brütting, A. P. Monkman, J. Phys. Chem. C 122 (2018) 29173–29179.
[32] D. Rezzonico, J. Photon. Energy 1 (2011), 011005.
[33] B. Perucco, N.A. Reinke, D. Rezzonico, E. Knapp, S. Harkema, B. Ruhstaller, Org. Electron. 13 (2012) 1827–1835.
[34] S. Zeder, C. Kirsch, U. Aeberhard, B. Blülle, S. Jenatsch, B. Ruhstaller, J. Soc. Inf. Disp. 28 (2020) 440–449.
[35] C. Xiang, W. Koo, F. So, H. Sasabe, J. Kido, Light Sci. Appl. 2 (2013) 1–7.
[36] Q. Zhang, T. Komino, S. Huang, S. Matsunami, K. Goushi, C. Adachi, Adv. Funct. Mater. 22 (2012) 2327–2336.
[37] J. Zhang, D. Ding, Y. Wei, H. Xu, Chem. Sci. 7 (2016) 2870–2882.
[38] T.D. Anthopoulos, J.P.J. Markham, E.B. Namdas, I.D.W. Samuel, S.C. Lo, P.L. Burn, Appl. Phys. Lett. 82 (2003) 4824–4826.
[39] J. Wang, J. Liu, S. Huang, X. Wu, X. Shi, C. Chen, Z. Ye, J. Lu, Y. Su, G. He, Y. Zheng, Org. Electron. 14 (2013) 2854–2858.
[40] F.S. Juang, C.C. Lee, J.Y. Chen, Y.H. Lin, D.W. Zhang, IOP Conf. Ser. Mater. Sci. Eng. 600 (2019).
[41] Y. Noguchi, Y. Miyazaki, Y. Tanaka, N. Sato, Y. Nakayama, T.D. Schmidt, W. Brütting, H. Ishii, J. Appl. Phys. 111 (2012).
[42] Y. Noguchi, Y. Tanaka, Y. Miyazaki, N. Sato, Y. Nakayama, H. Ishii, in: Physics of Organic Semiconductors, second ed., 2013, pp. 119–154.
[43] J.S. Bangsund, J.R. van Sambeek, N.M. Concannon, R.J. Holmes, Sci. Adv. 6 (2020) 1–11.
[44] P. Friederich, V. Rodin, F. von Wrochem, W. Wenzel, ACS Appl. Mater. Interfaces 10 (2018) 1881–1887.
[45] C. Murawski, K. Leo, M.C. Gather, Adv. Mater. 25 (2013) 6801–6827.
[46] B. van der Zee, Y. Li, G.J.A.H. Wetzelaer, P.W.M. Blom, Advanced Optical Materials, 2021.
[47] T. Kobayashi, A. Niwa, K. Takaki, S. Haseyama, T. Nagase, K. Goushi, C. Adachi, H. Naito, Physical Review Applied 7 (2017) 1–10.
[48] B. van der Zee, Y. Li, G.J.A.H. Wetzelaer, P.W.M. Blom, Adv. Opt. Mater. 9 (2021).
[49] H. van Eersel, P.A. Bobbert, R.A.J. Janssen, R. Coehoorn, Appl. Phys. Lett. 105 (2014) 1–6.
[50] A. Ligthart, X. de Vries, L. Zhang, M.C.W.M. Pols, P.A. Bobbert, H. van Eersel, R. Coehoorn, Adv. Funct. Mater. 28 (2018) 1–10.
[51] L. Zhang, H. van Eersel, P.A. Bobbert, R. Coehoorn, Chem. Phys. Lett. 662 (2016) 221–227.
[52] S. Wehrmeister, L. Jäger, T. Wehlus, A.F. Rausch, T.C.G. Reusch, T.D. Schmidt, W. Brütting, Physical Review Applied 3 (2015) 1–10.